The International Journal of Advanced Manufacturing Technology (2022) 121:765–784
https://doi.org/10.1007/s00170-022-09329-3

ORIGINAL ARTICLE

Numerical and experimental analysis of temperature distribution and melt flow in fiber laser welding of Inconel 625

Iskander Tlili[1] · Dumitru Baleanu[2,3,4] · S. Mohammad Sajadi[5,6] · Ferial Ghaemi[7] · Moram A. Fagiry[8]

Received: 8 October 2021 / Accepted: 5 May 2022 / Published online: 20 May 2022

Abstract

In these days, laser is a useful and valuable tool. Low input heat, speed, accuracy, and high controllability of laser welding have led to widespread use in various industries. Nickel-based superalloys are creep-resistant materials used in high-temperature conditions. Also, these alloys have high strength, fatigue, and suitable corrosion resistance. Inconel 625 is a material that is strengthened by a complex deposition mechanism. Therefore, the parameters related to laser welding affect the microstructure and mechanical properties. Therefore, in this study, the effect of fiber laser welding parameters on temperature distribution, weld bead dimensions, melt flow velocity, and microstructure was investigated by finite volume and experimental methods. In order to detect the temperature history during continuous laser welding, two thermocouples were considered at a distance of 2 mm from the welding line. The heat energy from the laser beam was modeled as surface and volumetric heat flux. The results of numerical simulation showed that Marangoni stress and buoyancy force are the most important factors in the formation of the flow of liquid metal. Enhancing the laser power to 400 W led to the expansion of the width of the molten pool by 1.44 mm, which was in good agreement with the experimental results. Experimental results also showed that increasing the temperature from 500 °C around the molten pond leads to the formation of a coarse-grained austenitic structure.

Keywords Laser welding · Superalloy · Temperature distribution · Microstructure · Mechanical properties

1 Introduction

Humans have long made various devices and equipment due to the desire to have a comfortable life. To build a complex mechanism, the need to connect different components has always been felt. In the past, due to lack of resources and sufficient knowledge in the use of resources, equipment, and technology used to connect materials has been very simple. However, over time, various methods of permanent and temporary connection emerged. One of the most essential methods used to connect parts permanently is welding and soldering. Various methods for welding parts have been proposed in recent years. However, with the advancement of technology in recent years, the use of high-power laser beams has been considered by researchers and artisans [1]. The laser welding method is suitable for welding various components due to the smaller heat-affected zone (HAZ), minimal thermal–mechanical distortion, low heat input, and good focusing characteristics. Also, reviewing the researchers' results in recent years, it is clear that the quality of laser welding depends on various process parameters such as laser

✉ Dumitru Baleanu
dumitru@cankaya.edu.tr

1 Physics Department, College of Science, Al-Zulfi, Majmaah University, AL-Majmaah 11952, Saudi Arabia

2 Department of Mathematics, Faculty of Arts and Sciences, Cankaya University, Ankara, Turkey

3 Lebanese American University, 11022801 Beirut, Lebanon

4 Department of Medical Research, China Medical University Hospital, China Medical University, Taichung, Taiwan

5 Department of Nutrition, Cihan University-Erbil, Erbil, Kurdistan Region, Iraq

6 Department of Phytochemistry, SRC, Soran University, Soran, KRG, Iraq

7 Department of Chemical and Process Engineering, Faculty of Engineering and Built Environment, Universiti Kebangsaan Malaysia (UKM), 43600 Bangi, Selangor, Malaysia

8 Radiology and Medical Imaging Department, College of Applied Medical Sciences, Prince Sattam bin Abdulaziz University, Al-Kharj, Saudi Arabia

power, pulse duration, frequency, focal length, and welding speed [2, 3]. Also, the type of parts used in the laser welding process is very essential. One of the most widely used materials in recent years in all automotive, aerospace, food, oil and gas industries, and pollution control equipment is Inconel superalloys [4]. One of the most important and widely used Inconel superalloys is Inconel 625. This metal has excellent resistance to corrosion at high temperatures and acidic environments. It is also a suitable metal for welding due to its unique mechanical properties [5]. In recent years, the study of metal bonding by numerical and experimental methods in the laser welding process has always been of interest to researchers.

Liu et al. [6] investigated the five kinds of thermal cycle, with different peak temperatures ranges in welding of Inconel 617 and simulated HAZs with same heating and cooling rate. The results indicated that the micro-hardness and average grain size of simulated HAZs have no obvious variation compared to the BM. Azari et al. [7] analyzed the temperature distribution and fusion zone microstructure in an Inconel 625 superalloy laser welding. The findings indicated that the temperature distribution changes of laser parameters such as welding speed, nozzle distance, beam displacement, and laser power, which led to a change in the molten pool's depth and width. It was also found that increasing the power of the laser has a significant effect on increasing the temperature. Faraji et al. [8] investigated heat and mass transfer using numerical modeling of fluid flow in a dissimilar laser welding process of Ti6Al4V and Inconel 718. The findings proved that the proposed numerical model has a good agreement with experiments. Madhankumar et al. [9] analyzed the laser welding parameters' effect on the tensile strength of Inconel 718 and duplex 2205 stainless steel alloys. By examining the laser parameters, the desired ultimate tensile strength was obtained from the analysis of variance to gain the weld connection optimization. Thejasree et al. [10], in an experimental–numerical study, investigated the laser welding parameters effect on the molten pool and welding geometry of Inconel 625. With the simulation performed by SYSWELD software, it was found that the experimental and simulation results are very close according to the thermal, microstructural, and mechanical analysis. The effect of laser power and welding time was also reported as effective parameters. Ahmad et al. [11], in the fiber laser welding process of duplex 2205 and Inconel 625 alloys, investigated the effect of different heat inputs on the microstructure and welding geometry of the welding area. The results showed that by reducing the energy input, the molten pool's width was reduced, and the mechanical properties of the joint area were improved. In a laser welding process, Voropaev et al. [12] investigated the effects of heat treatment on Inconel 718 alloy. The results showed a significant effect of heat treatment on the weld metal structure and complete phase transformations occurred. Srikanth and Parthiban [13], in a laser welding process, studied the welding heat effect on the microstructure of Inconel 625. The results of the microstructure study in the fusion zone showed that the grain size was affected by the welding heat and the laser power. Cheepu et al. [14], in a laser welding process, investigated the effect of laser parameters on the mechanical properties of high tensile steel and Inconel 718. The results illustrated that laser power had a significant effect on the strength and weld's mechanical properties. In a laser welding process, Sharma et al. [15] surveyed the laser parameters' effect on the melting zone. The results indicated that the height of the surface reinforcement and the surface of the weld melting zone decreased with increasing scanning speed.

Devendranath Ramkumar et al. [16] obtained the optimal process parameters for laser welding of Inconel alloy 718 alloys and martensitic stainless steel. The outcomes showed that by using the desired welding speed (1500 mm/min), a fusion zone without porosity and an ideal keyhole could be achieved. Mishra et al. [17] investigated the joint area's microstructure and mechanical properties of Inconel 625 and S.S 316 in a laser welding process. The results illustrated that the microstructure of the weld zone near Inconel 625 was columnar dendrites, while near the S.S 316, metal was predominantly cellular. Li et al. [18] evaluated the quality of laser welding performed by fiber laser on Inconel 718. The results indicated that the welding quality and appearance could be bright and smooth by reducing the ambient pressure. Also, the study of plasma distribution proved that a smaller area of plasma led to an increase in the laser energy absorption efficiency, which ultimately led to an increase in the depth of penetration. Hernando et al. [19] developed a numerical model for predicting weld geometry and joint area microstructure of Inconel 718 in the laser welding process. The results proved that there was a good agreement between the experimental model and the proposed numerical model, and the most important parameters affecting the welding were the laser power and feed rate. In another study, Hernando et al. [20] simulated and predicted the parameters affecting the welding of Inconel 718 alloy concerning the wobbling strategy. This strategy showed that a wide range of welds could be covered by combining elliptical and linear motions. Jelokhani-Niaraki et al. [21] investigated the optimal parameters of the Inconel 625 laser welding process using the response surface method (RSM). The finding indicated that the maximum welding strength was obtained when the values of laser power, laser speed, and spot size were 260 W, 1.2 mm/s, and 180 μm, respectively. Ebrahimi et al. [22] used the Gaussian optics theory to investigate the thermal effects of Inconel 625 and 316 stainless steel welding in keyhole formation. The results illustrated that this volumetric model was suitable for simulating heat flux profiles and could depict the actual conditions well. Janasekaran et al.

Table 1 Chemical composition of Inconel 625 [7]

Composition	C%	Nb%	Cr%	Nb%	Mn%	Fe%	Ti%	Si%	Mo%	V%	Si%	W%	Ni%
Weight	0.082	3.5	22.85	3.5	0.11	4.81	0.19	0.1	8.1	0.01	0.1	0.014	59.6

[23] evaluated the effect of overlap factor and laser welding speed on the laser welding of Inconel 600 and Ti6Al4V. The results indicated that the optimal parameters to achieve a suitable strength were equal to an overlap factor of 50%, speed of welding of 40 mm/s, and laser welding power of 250 W. Ren et al. [24] conducted a comparative study between CO_2 laser welding methods and fiber laser welding of Inconel 617 alloy. The outcomes illustrated that to achieve a complete melting penetration in the welding process, fiber laser was more efficient, and the appearance of the weld bead geometry was also different. Numerical simulation of the weld profile and weld pool dynamics according to the variation of temperature field for aluminum alloy was conducted by Duggirala et al. [25]. Evidently, 3D modeling of the melt pool dimensions has been accurately done and the volume of the melt pool was predicted according to the thermal model results. Besides, the dynamics of an unstable keyhole, Marangoni convection, and buoyancy forces effects on the molten pool dimensions was considered. This numerical model results were validated with an experimental study with a maximum of 5% and 3% error in the depth and width, orderly.

By examining the effect of continuous wave laser welding parameters on the temperature gradient in the molten pool, the thermal stress in the workpiece can be controlled, and the possibility of thermal fatigue can be reduced. For this purpose, in this study, an experimental and numerical study of Inconel 625 sheet laser welding was conducted. The main aim of this study is to investigate the effect of laser heating cycle on the extension of melt pool dimensions and the influence of cooling cycle on the microstructural changes of the fusion zone and adjacent areas by considering the material properties temperature dependent. Due to the significant effect of melt flow and shear stress caused by Marangoni flow on the temperature gradient and dimensions of the weld bead, the finite volume method was used to discretize the conservation equation.

2 Experimental procedure

Fiber laser at continuous mode with a maximum nominal output power of 500 W and Raytools BW240 laser welding head with copper side delivery gas nozzle was used for welding experiments. Argon gas at a constant pressure of 35 psi was blown to the welding area to protect the welding region. The temperature measuring at the location of 2 mm away from the laser beam's center was done by K-type thermocouples. The materials of welding were Inconel 625 with 1.5-mm thickness. The sample's material chemical properties are illustrated in Table 1.

Detailed actual experimental setup including CNC, laser welding head, workpiece fixture, thermocouples, and data logger USB4718 and welded workpiece is observed in Fig. 1. For thermocouple placement, the special groove was

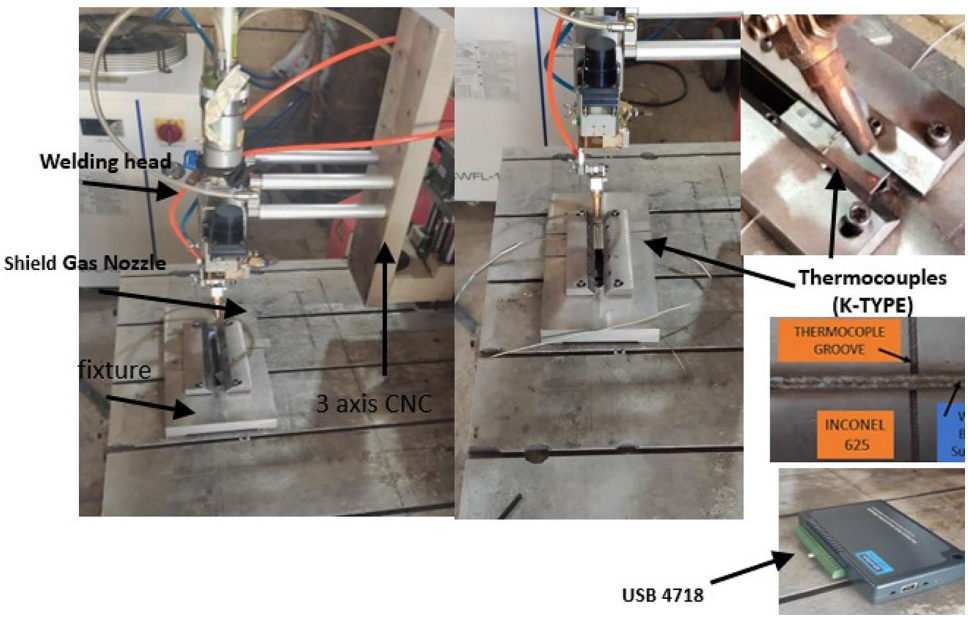

Fig. 1 Actual view of the experimental laser welding setup

engraved using EDM. After mounting thermocouples, both the workpiece and thermocouples simultaneously clamped via fixture chuck. The laser beam moves through CNC traverse axis and argon gas was blown through nozzle. The thermocouples were attached to the DAQ card to convert the analog signal to digital.

Figure 2 shows a schematic of the laser welding process and the dimensions of the pieces. In order to investigate the various laser welding parameters and validate the results, the time history of temperature, according to Fig. 2, was obtained around the center of the beam.

The Olympus optical microscope under the ASTM E883-11 standard was used for microstructure images metallurgical analysis preparation. The samples were etched under ASTM E3-11 standard, and the microstructure was analyzed with TESCAN MIRA3 FESEM.

3 Numerical simulation

The temperature gradient and liquid metal's flow in the molten pool have a direct relation with the quality and mechanical properties of the welded metal. Therefore, predicting the parameters affecting the heat transfer and fluid flow can increase the welding quality and reduce the costs. In order to numerical simulation of continuous laser welding, a finite volume transient numerical model was used. A numerical code was also used to define the thermal model and the thermophysical properties with temperature variation. The number of grid elements after the grid study was considered to be 421875.

3.1 Governing equations

The discretization of the equations was considered according to these assumptions:

- The flow of fluid was considered incompressible, Newtonian, and laminar.
- The molten pool's surface was considered flat.
- Vaporization of liquid metal was ignored.
- The initial temperature of 25 °C was considered.

Gaussian heat source and heat flux were utilized to simulate the absorbed energy. One of the main objectives of this paper is to evaluate the accuracy of 5 different thermal models for numerical simulation of Inconel 625 laser welding based on different shapes which are shown in Fig. 3. The model basic equations are described in Eqs. (1)–(5) [26, 27].

$$q_s(x,y) = \frac{3f_1\eta p}{\pi r_s^2}\exp\left(-3\frac{\left(x^2+y^2\right)}{r_s^2}\right) \quad \text{surface heat flux} \tag{1}$$

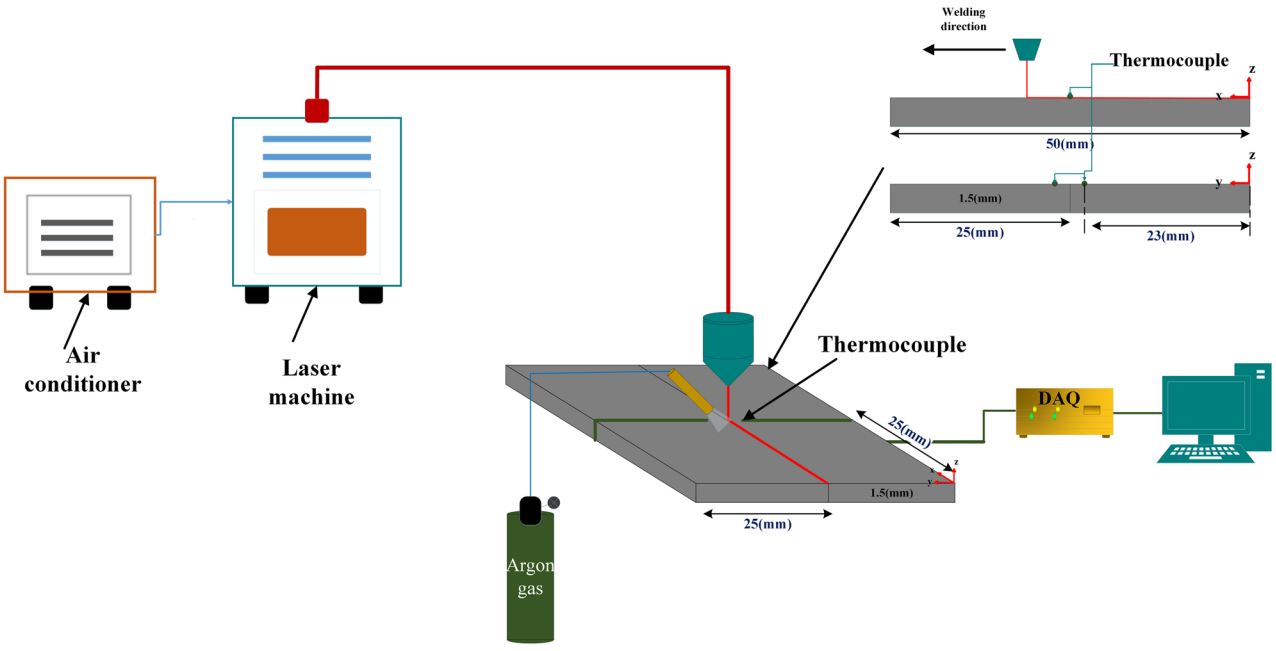

Fig. 2 Schematic configuration of the laser welding process

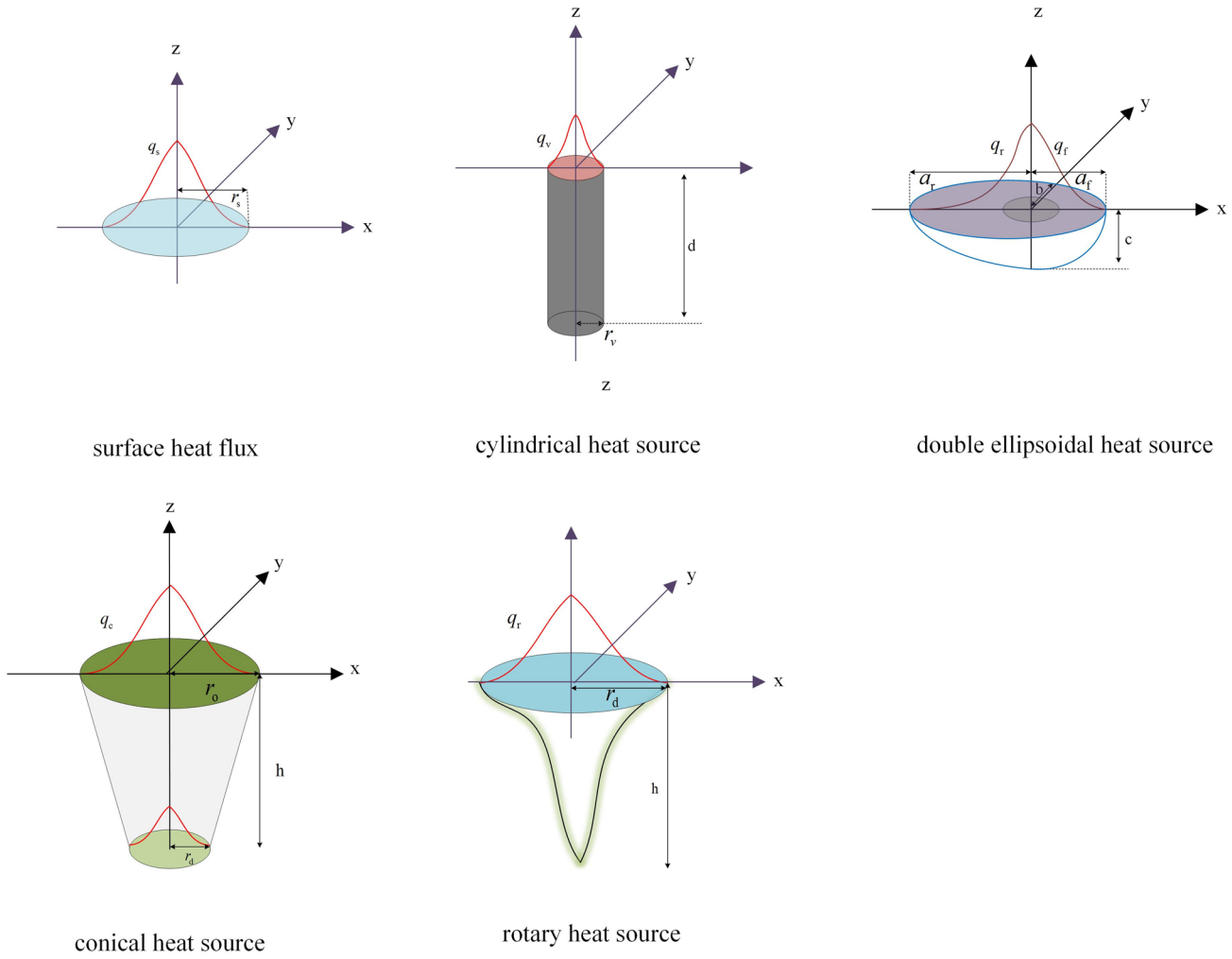

Fig. 3 Various thermal models for numerical simulation

$$q_v(x,y,z) = \frac{6f_2\eta p}{\pi r_v^2 d}\exp\left(-3\frac{(x^2+y^2)}{r_v^2}\right)\left(\frac{mz+r_v}{md+2r_v}\right) \quad \text{cylindrical heat source} \tag{2}$$

$$q_f(x,y,z) = \frac{6\sqrt{3}f_f\eta p}{a_f bc\pi\sqrt{\pi}}\exp\left(-3\left(\frac{x^2}{a_f^2}+\frac{y^2}{b^2}+\frac{z^2}{c^2}\right)\right)$$
$$q_f(x,y,z) = \frac{6\sqrt{3}f_f\eta p}{a_f bc\pi\sqrt{\pi}}\exp\left(-3\left(\frac{x^2}{a_f^2}+\frac{y^2}{b^2}+\frac{z^2}{c^2}\right)\right) \quad \text{double ellipsoidal heat source} \tag{3}$$

$$q_c(x,y,z) = q_o \exp\left(-2\frac{(x^2+y^2)}{r_o - \frac{z}{h}(r_o - r_d)}\right) \quad \text{conical heat source} \tag{4}$$

$$q_r(x,y) = \frac{f\eta p}{\pi r_d^2 h}\exp\left(-3\frac{(x^2+y^2)}{r_d^2}\right)\left(1-\frac{z}{h}\right) \quad \text{rotary heat source} \tag{5}$$

In Eqs. (1)–(5), q_s, q_v, q_f,q_r, and q_c are the surface heat flux, cylindrical volumetric heat flux, ellipsoid heat source at the front of the laser beam, ellipsoid heat source at the rear of the laser beam, and conical heat source, respectively. p is the laser power, f,f_1,f_2 are energy distribution coefficients, and f_f,f_r are heat source distribution coefficients ellipsoid at the front and rear of the beam, respectively. q_o in Eq. (4) is laser beam energy and q_r in Eq. (5) is rotary heat source. Also, a_f, a_r, b, c are parameters for determining the size and shape of the ellipse to consider the heat source distribution. d and h indicate the height of the cylindrical, conical, and rotary heat source and r_s and r_v represent the radius of the surface heat flux and the cylindrical heat source, respectively. r_o and r_d are the radius of the conical heat source at the surface and depth and r_d the radius of the rotary heat source, m is the coefficient of Gaussian damping, and η is the coefficient of absorption [28, 29].

Continuity equation:

$$\frac{\partial \rho}{\partial t} + \nabla.(\rho \vec{U}) = 0 \tag{6}$$

Momentum equation:

$$\frac{\partial\left(\rho\vec{U}\right)}{\partial t} + \nabla.\left(\rho\vec{U}\vec{U}\right) = -\nabla \mathrm{p} + \nabla.\left(\mu\nabla\vec{U}\right) + \rho\vec{g} - \frac{\mu}{K}\left(\vec{U}\right) \tag{7}$$

Energy equation:

$$\frac{\partial(\rho H)}{\partial t} + \nabla.\left(\rho\vec{U}H\right) = \nabla.(k\nabla T) + q \tag{8}$$

where $\rho, H, t, p, \vec{U}, k, \vec{g}, K,$ andμ are density, total enthalpy, time, pressure, vector of velocity, coefficient of thermal conductivity, gravity acceleration, coefficient of Darcy resistance, and dynamic viscosity, respectively.

3.2 Boundary conditions

The boundary condition at the surface:

$$k\frac{\partial T}{\partial \vec{n}} = -\varepsilon\sigma\left(T^4 - T_\infty^4\right) - h\left(T - T_\infty\right) + q_s \tag{9}$$

where ε is the coefficient of emission, σ is the coefficient of Stefan–Boltzmann, T_∞ is the surrounding temperatures, and h is the coefficient of convection heat transfer.

Shear stress due to surface tension gradient:

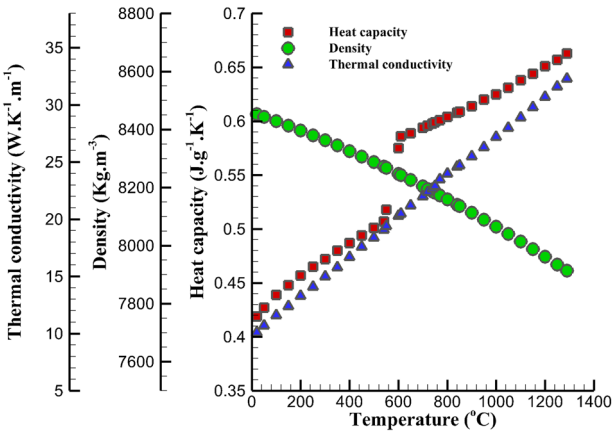

Fig. 4 Thermophysical properties as a function of temperature [30–32]

$$\mu\frac{\partial u}{\partial z} = -\frac{\partial \gamma}{\partial T}\frac{\partial T}{\partial x} \tag{10}$$

$$\mu\frac{\partial v}{\partial z} = -\frac{\partial \gamma}{\partial T}\frac{\partial T}{\partial y} \tag{11}$$

The boundary condition on the lower and lateral surfaces was expressed as follow:

$$k\frac{\partial T}{\partial \vec{n}} = -\varepsilon\sigma\left(T^4 - T_\infty^4\right) - h\left(T - T_\infty\right) \tag{12}$$

3.3 Thermophysical properties

High-temperature variations during laser welding of Inconel alloy 625 lead to significant changes in thermophysical properties. Therefore, the correct determination of the properties of the considered material could lead to accurate modeling of the laser welding process. For this purpose, some thermophysical properties as a function of temperature are shown in Fig. 4. Also, other thermophysical properties are listed in Table 2.

Table 2 Thermophysical properties of Inconel 625 [30–37]

Nomenclature	Symbol	Value	Unit
Solidus temperature	T_s	1563	k
Liquidus temperature	T_l	1623	k
Ambient temperature	T_∞	298	k
Melting latent heat	L_m	227×10^5	Jkg^{-1}
Surface tension gradient	A_σ	−0.00011	$Nm^{-1}k^{-1}$
Stefan-Boltzmann constant	σ	5.67×10^{-8}	$Wm^{-2}k^{-4}$
Dynamic viscosity	μ	0.0072	$kgm^{-1}s^{-1}$

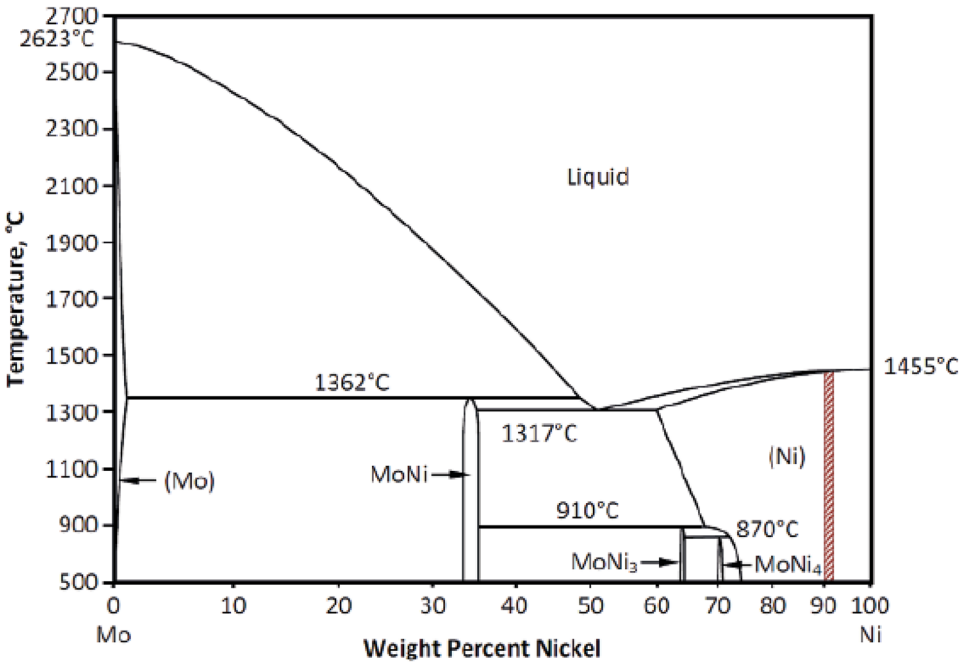

Fig. 5 Phase diagram of nickel base alloy [38]

The phase diagram of nickel base alloys is illustrated in Fig. 5. Various phase changing of material depended to temperature including solidification liquid and different phase changes could be observed according to nickel weight percentage of alloy.

4 Results and discussions

After discretizing the continuity, momentum, and energy governing equations as a finite volume method and considering the boundary conditions, three-dimensional modeling of the welding speed effect and laser power on the temperature distribution, velocity, and weld bead dimension was done. The considered parameters to investigate the temperature history, velocity, and fusion zone during the continuous wave laser welding process are given in Table 3. In all cases, the focal position was considered at the surface of the pieces.

Table 4 and Fig. 6 show a clear comparison of the molten pool dimensions in different thermal model conditions for numerical and experimental as well (power = 350 W and welding speed = 500 mm/min). As can be seen, the combination of surface heat flux and cylindrical heat source in the numerical simulation had the minimum discrepancy with the experimental result. Besides, in laser welding, the beam absorption could be divided into reverse energy absorption at the surface of the molten pool and the Fresnel absorption on the wall of the keyhole [39, 40]. Therefore, considering the surface and volumetric heat flux can provide an accurate prediction of the temperature distribution. Figure 6b, d, and e have had the highest discrepancy and roughly predicted the melt pool widths. Figure 6c, f had acceptable accuracy for estimation depth and width. The finest estimation goes to the model (combination of surface heat flux and cylindrical heat source) which results presented in Fig. 6f for both of width and depth including fusion zone and HAZ region.

Table 3 Laser welding parameters for numerical simulation

Sample	Welding speed (mm/min)	Power (W)
1	300	350
2	400	350
3	500	350
4	300	300
5	300	400

According to the simulation results obtained from Fig. 6, the most suitable heat flux (combination of surface heat flux and cylindrical heat source) is presented in Eqs. (13) and (14) and Fig. 7.

$$q_s(x,y) = \frac{3f_1\eta p}{\pi r_s^2}\exp\left(-3\frac{\left(x^2+y^2\right)}{r_s^2}\right) \tag{13}$$

$$q_v(x,y,z) = \frac{6f_2\eta p}{\pi r_v^2 d}\exp\left(-3\frac{\left(x^2+y^2\right)}{r_v^2}\right)\left(\frac{mz+r_v}{md+2r_v}\right) \tag{14}$$

4.1 Temperature distribution

Predicting the temperature distribution and HAZ can help to control the primary microstructure. Hence, the temperature

Table 4 Comparison of molten pool dimensions obtained from numerical simulation with experimental results (width and depth are 0.94 and 0.62 mm, respectively)

Thermal model	Numerical simulation results		Differences with experimental results (%)	
	Width (mm)	Depth (mm)	Width	Depth
Surface heat flux	1.02	0.44	8.51	29.03
Cylindrical heat source	0.75	0.68	20.21	9.68
Double ellipsoidal heat source	0.82	0.59	12.77	4.84
Conical heat source	0.63	0.58	32.98	6.45
Rotary heat source	0.68	0.70	27.66	12.90
Surface heat flux + cylindrical heat source	0.89	0.65	5.32	4.84

history was obtained at different welding speeds and laser powers. Figure 8 shows the time history of temperature at different welding speeds within 2 mm of the center of the beam. As can be seen, with increasing the speed of movement of the thermal model due to the reduction of power density absorption time, the temperature decreased significantly. So that with increasing the speed of movement laser head from 300 to 500 mm/min, the temperature decreased by approximately 160 °C. Also, the results obtained from numerical simulations were in good agreement with the results of experiments, which indicated the correct determination of the Gaussian heat source and heat flux and thermophysical properties. Figure 9 indicates the temperature variation versus time at different laser powers. It can be concluded that, with enhancing the laser power by 100 W, the maximum temperature around the fusion zone increased by

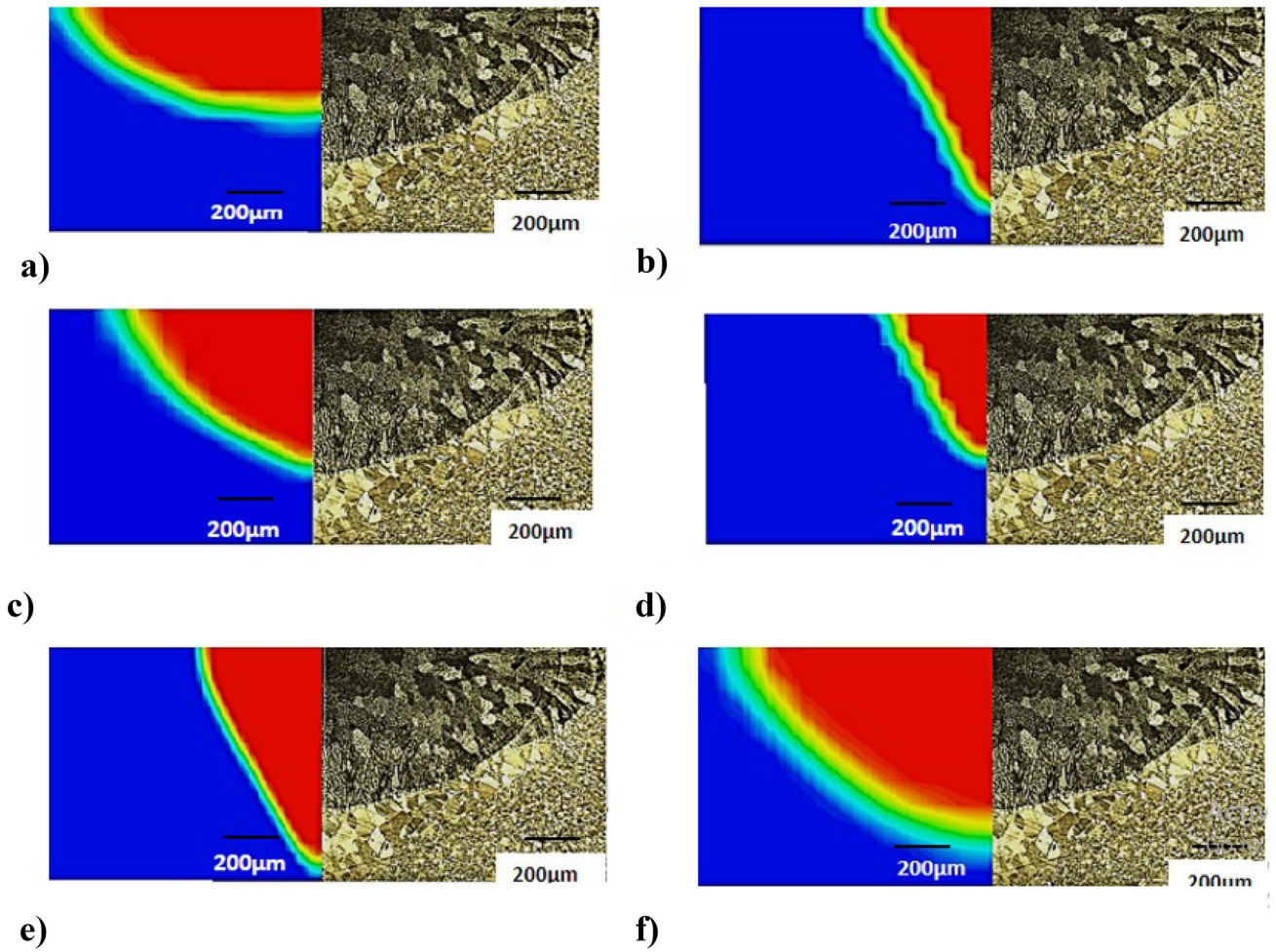

Fig. 6 Different thermal model temperature distribution compared with experimental data at laser power of 350 W and welding speed of 500 mm/min: (**a**) surface heat flux, (**b**) cylindrical heat source, (**c**) double ellipsoidal heat source, (**d**) conical heat source, (**e**) rotary heat source, and (**f**) surface heat flux + cylindrical heat source

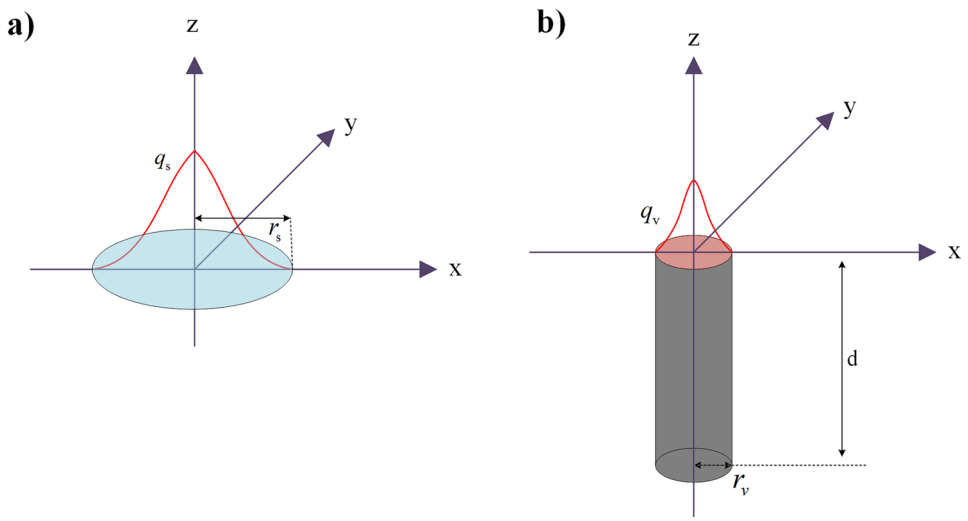

Fig. 7 Configuration of thermal modes: (**a**) heat flux, (**b**) cylindrical heat source

about 120 °C due to the enhanced power density. It is also concluded that by enhancing the power density, the maximum temperature was obtained at a higher time.

Considering that there is no change in the microstructure of Inconel 625 alloy up to a temperature of 700 °C and the starting the formation of γ (Ni3Nb) from 700 °C; by determining the temperature distribution on the workpiece's surface, the range of the HAZ can be identified.

Figure 10 illustrates that the temperature contour at different welding speeds on the workpiece's surface. As can be seen, as the speed of movement of the thermal model increased due to the reduction of heat energy absorption time, the heat penetration to the around decreased. In other words, as the welding speed increased, the isothermal line became an ellipsoid shape which led to a reduction in the HAZ and liquid volume of metal.

This can be explained by Fig. 11. It can be concluded that different points along the *y*-axis in a certain section reach their peak temperature at different times. Farther points have lower peak temperature at same time. Maximum temperatures are shown at different points with n–n curve. As the laser beam travels faster, the n–n curve bends further at the surface due to the reduced residence time of the laser beam. The same factor leads to the constant temperature lines on the surface of the workpiece became ellipsoid at high speed (Fig. 11b).

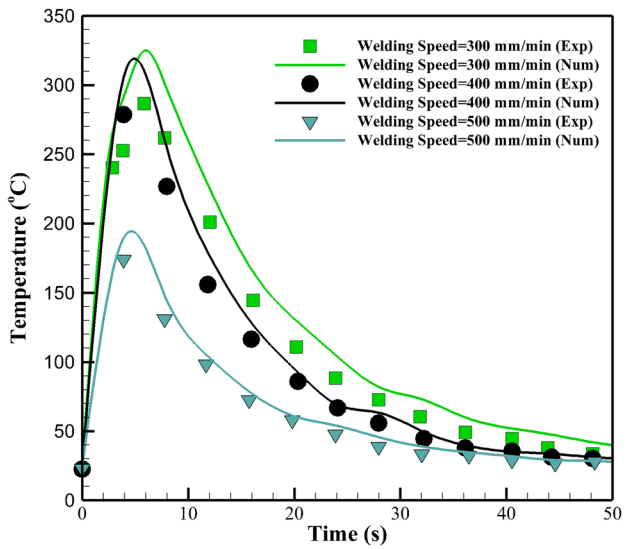

Fig. 8 Comparison of temperature distribution versus time in simulated and experimental results for different welding speeds

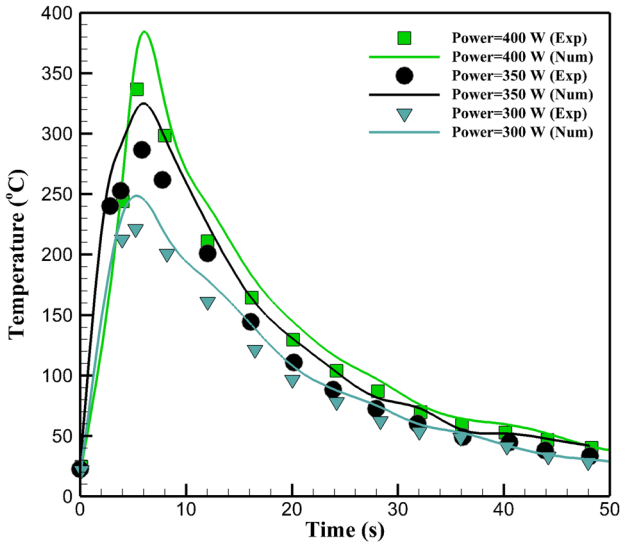

Fig. 9 Comparison of temperature distribution versus time in simulated and experimental results for different laser powers

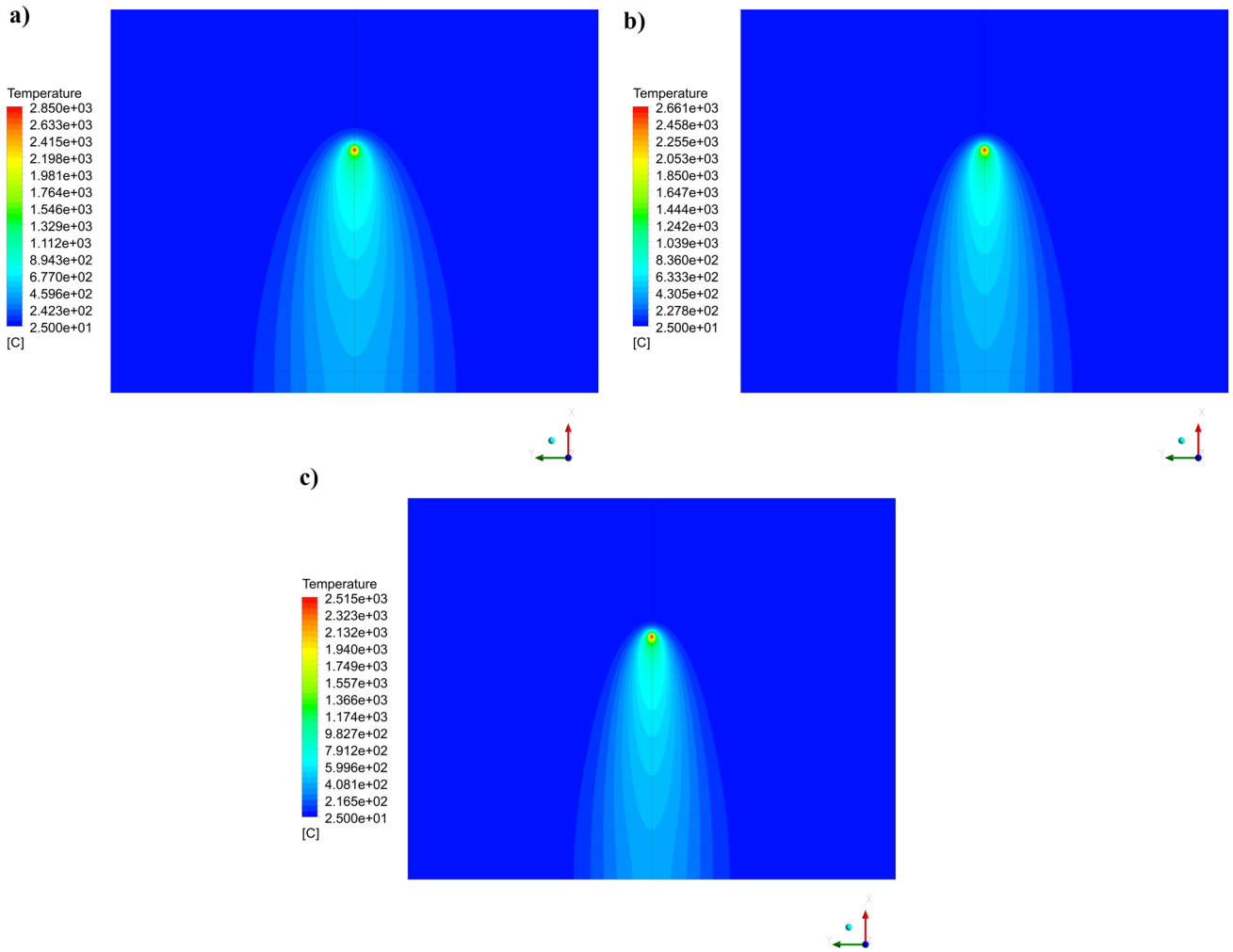

Fig. 10 Temperature contour on the workpiece's surface at different welding speeds, (**a**) 300 mm/min, (**b**) 400 mm/min, and (**c**) 500 mm/min

Figure 12 indicates the effect of laser power on the temperature contour of sheet surface at a distance of 25 mm from the beginning of the welding. Because the thermal conductivity coefficient of Inconel 625 is relatively low, this caused less heat penetration to other parts of the workpiece. On the other hand, the HAZ was increased because the heat concentration was higher in the areas close to the laser beam. As shown in Fig. 12, increasing the continuous laser power has no effect on the shape of the temperature field, and only the workpiece experienced a higher constant temperature line.

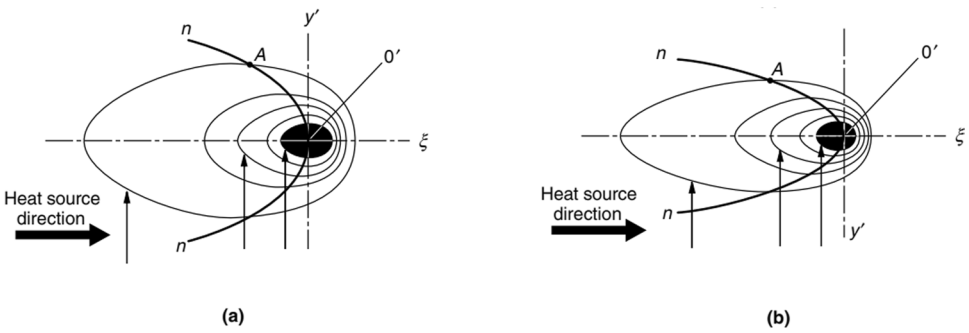

Fig. 11 Schematic temperature distribution as a function of welding speed variation, (**a**) low speed, (**b**) high speed [41]

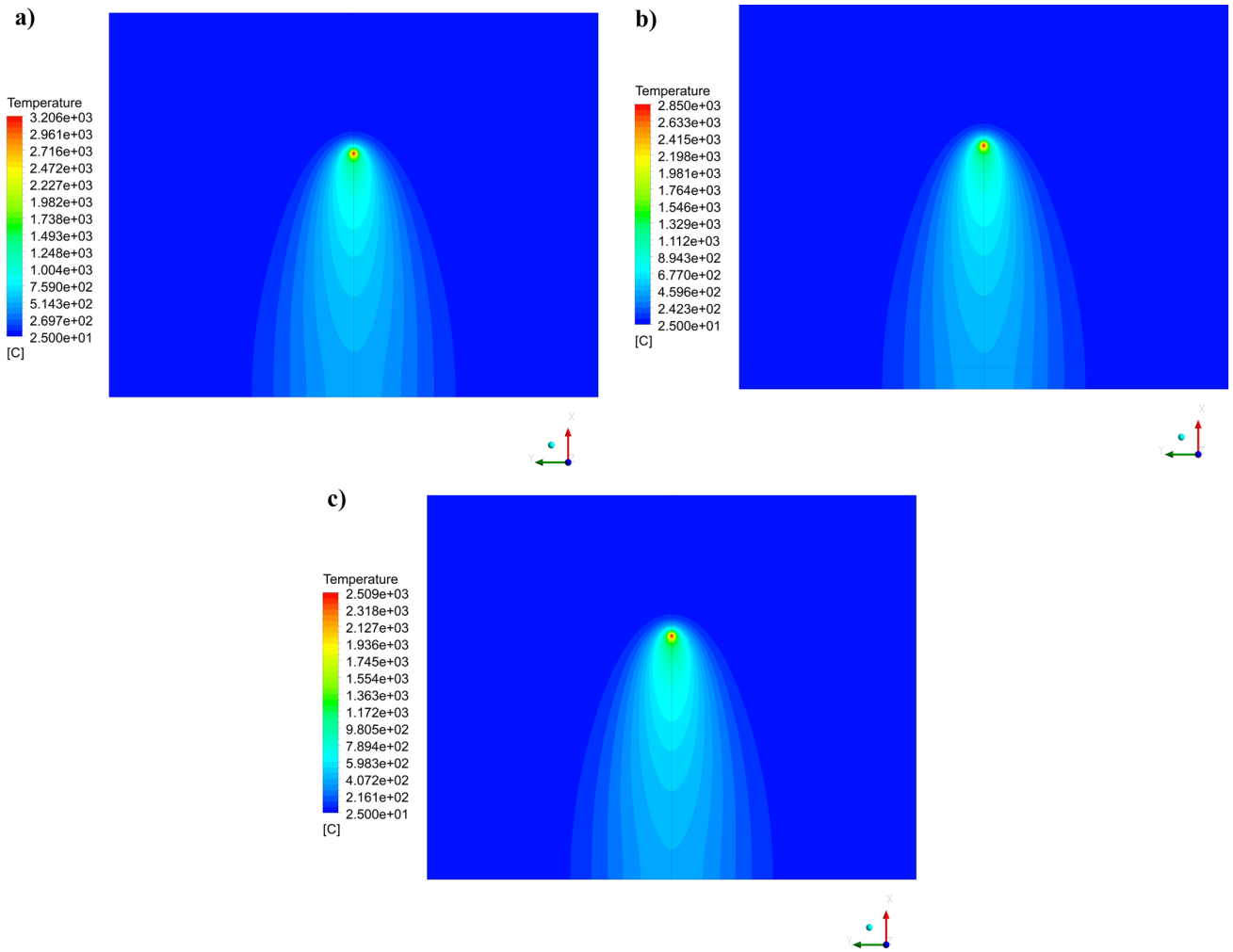

Fig. 12 Temperature contour on the workpiece's surface at various laser powers, (**a**) 400 W, (**b**) 350 W, and (**c**) 300 W

4.2 Velocity distribution

Due to the active elements in the metals, their surface tension may increase or decrease at the molten pool's surface with increasing temperature. So that if the surface tension gradient was negative, the flow would move from the high-temperature region to the low-temperature region, and a Marangoni flow will be formed. Inconel alloy is one of the metals that have a negative Marangoni coefficient. As can be seen in Figs. 13 and 14, the flow has been created across the cross-section of the workpiece from the laser beam's center to the mushy zone.

Figure 13 shows that with increasing the speed due to decreasing temperature and Marangoni force on the workpiece's surface, shear stress decreased, which led to a decrease in molten flow velocity. Figure 14 indicates the vector of velocity in various continuous wave laser powers. As the laser power increased, due to the enhance of temperature gradient and surface tension gradient, the velocity of the molten flow increased and led to an increase in the role of convective heat transfer in the molten pool.

4.3 Shape and dimensions of the molten pool

Predicting the dimensions of the weld bead in different laser parameters can lead to the appropriate connection of the two sheets. Evidently, the major aim of numerical simulation in this study was evaluation of the temperature distribution with acceptable accuracy to reach a reasonable simulation results close to the experimental results. Although some simplifications considered in the thermal model, some terms such as evaporation, cavitation, and formation of plasma plume are neglected. In laser welding process, the amount of absorbed laser beam to the material would be highly dependent on material phase such as solid,

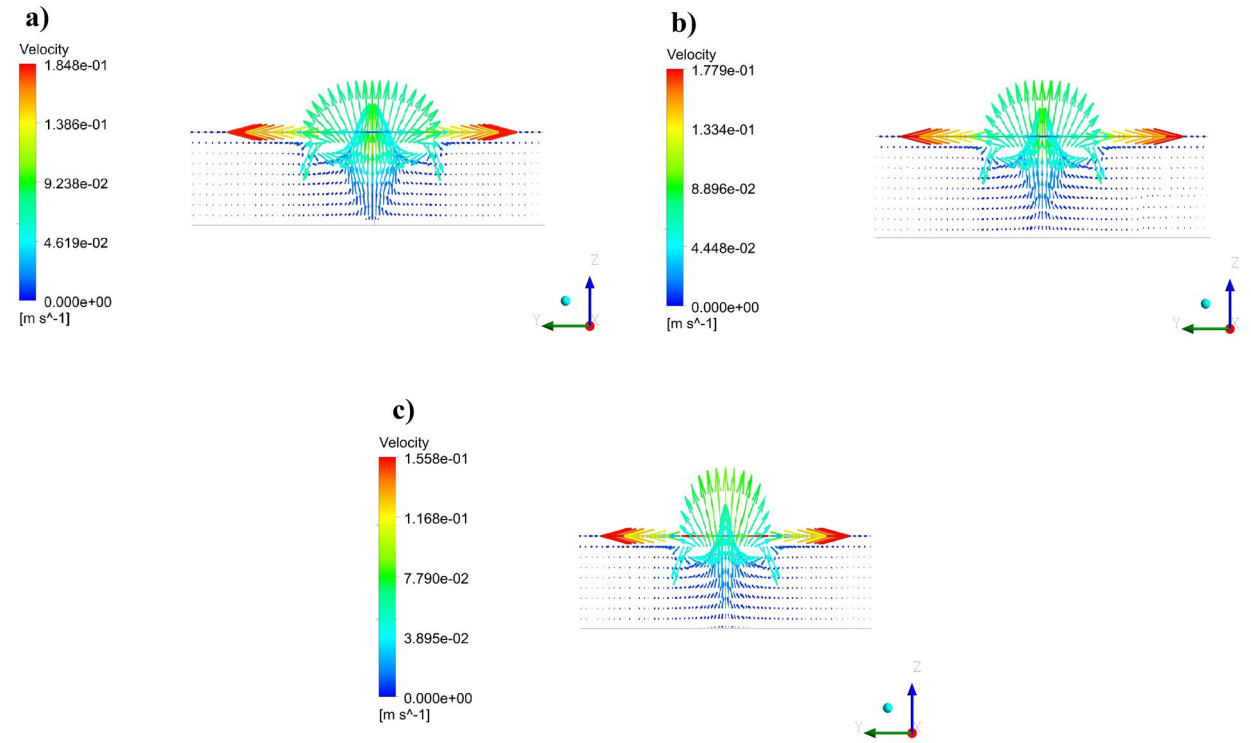

Fig. 13 Vector of velocity at the cross-section of the workpiece at various welding speeds, (**a**) 300 mm/min, (**b**) 400 mm/min, and (**c**) 500 mm/min

liquid, or gas. Among different parameters of laser welding, the laser beam energy density plays a crucial role on the created temperature and melt pool dimensions. The laser power level significantly effects on the creation of melt pool and thereby extension of depth, width, and surface of the melt pool. The temperature-dependent material density

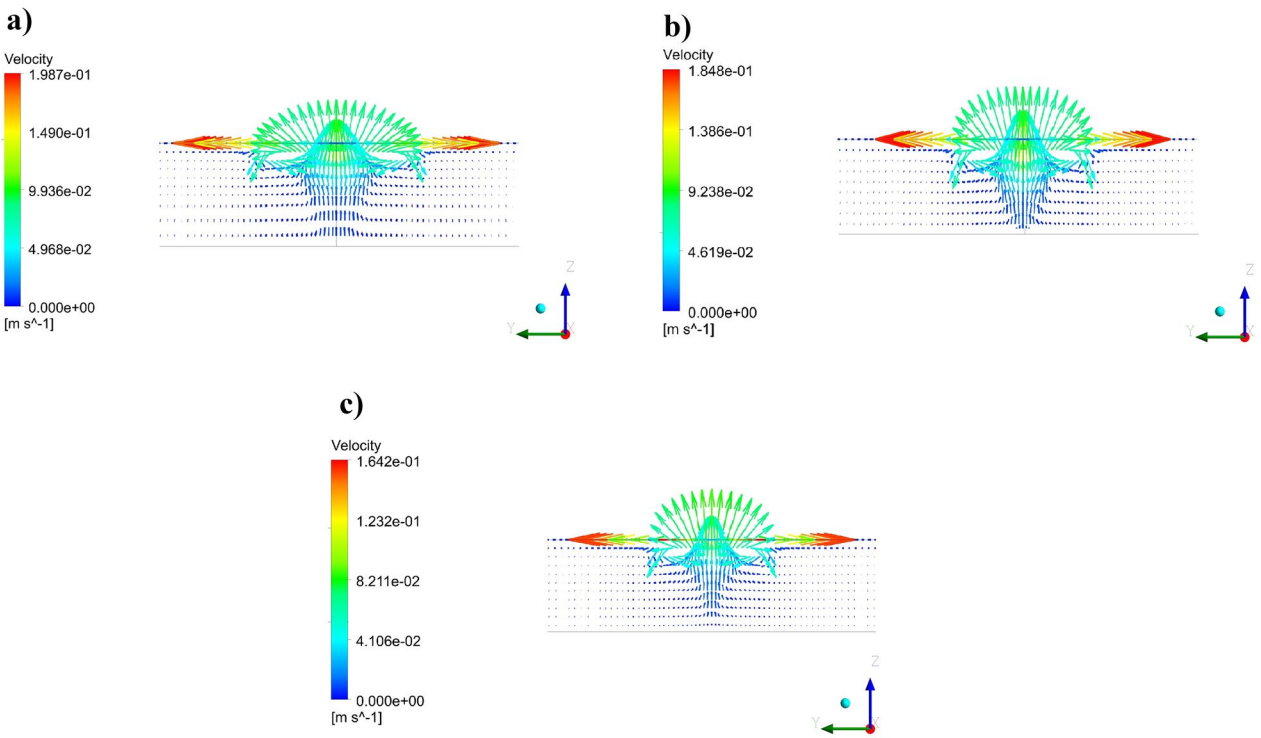

Fig. 14 Vector of velocity at the workpiece's cross-section at various laser powers, (**a**) 400 W, (**b**) 350 W, and (**c**) 300 W

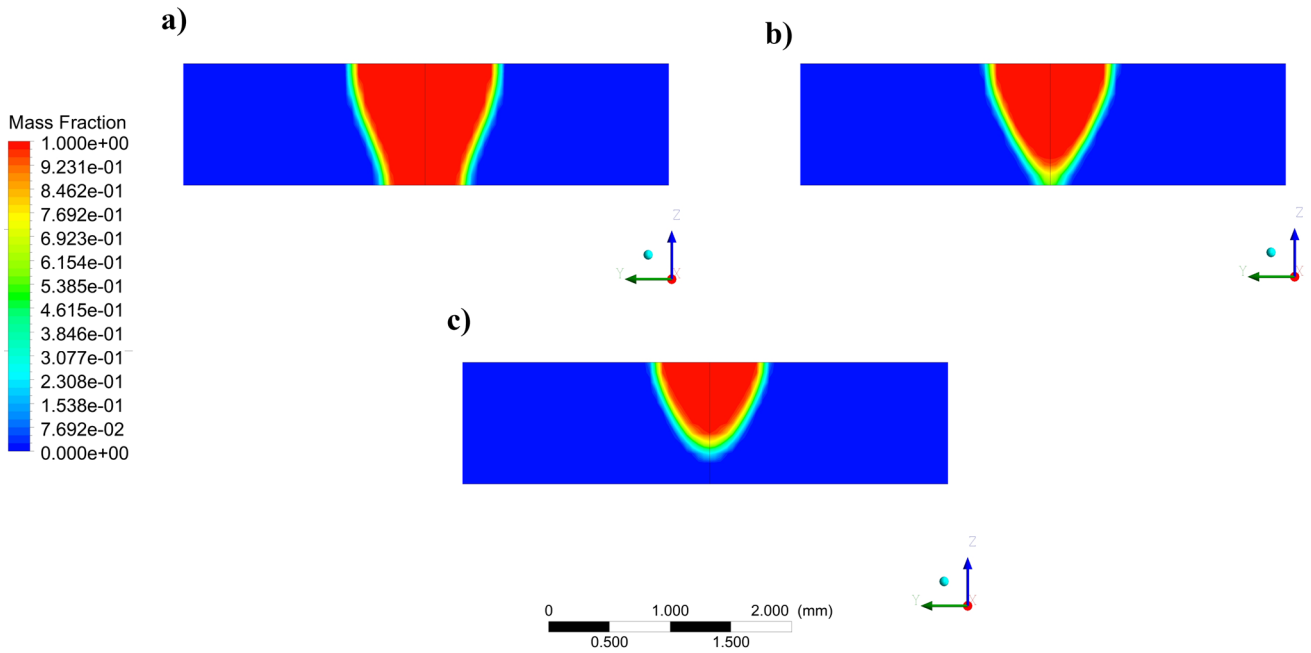

Fig. 15 The molten pool's shape at various welding speeds, (**a**) 300 mm/min, (**b**) 400 mm/min, and (**c**) 500 mm/min

and thermal conductivity influentially affect the thermal model predicted temperature and flow of the melted material. In this case, the high temperature alloys such as nickel base superalloys could have the closest results to the real experiments because of having higher melting point and lower thermal conductivity. On the other hand, the reflective metals such as aluminum, magnesium, and brass generally create a higher difference with experiment due to high reflection rate related to the laser beam and low melting point that lead to the evaporation of molten metal and cavitation as well. Figures 15 and 16 show the mass fraction of the melt at different welding speeds and laser powers, respectively. As seen in these figures, the amount of created melt was significantly reduced by increasing the

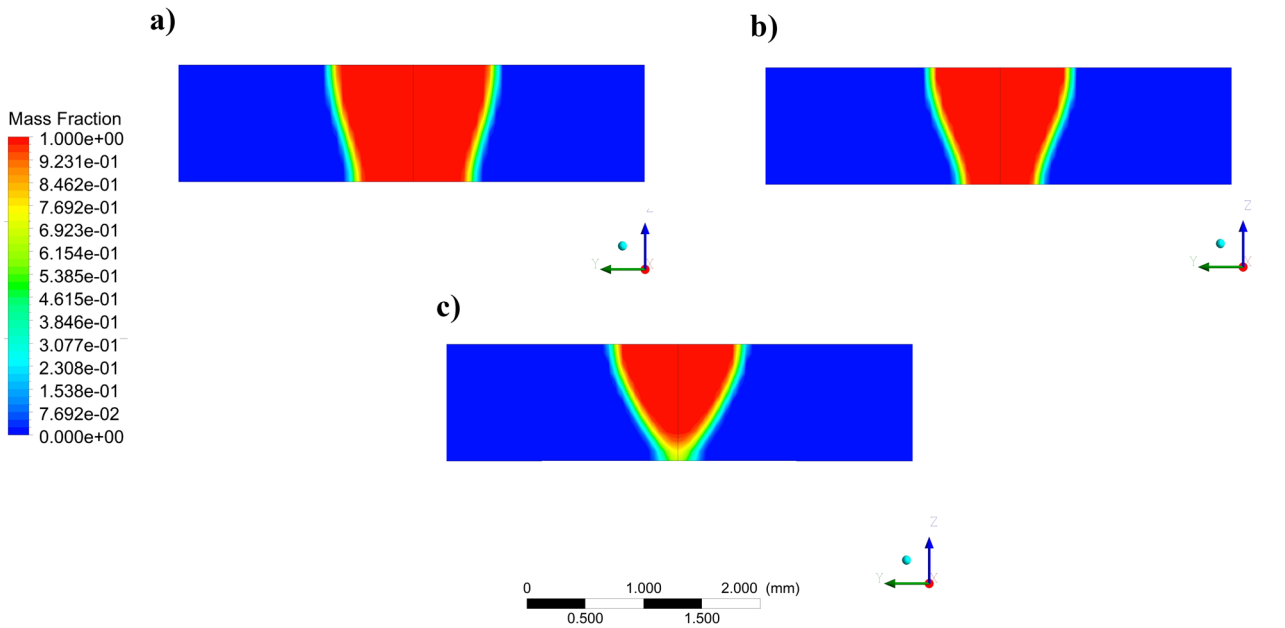

Fig. 16 The molten pool's shape at various laser powers, (**a**) 400 W, (**b**) 350 W, and (**c**) 300 W

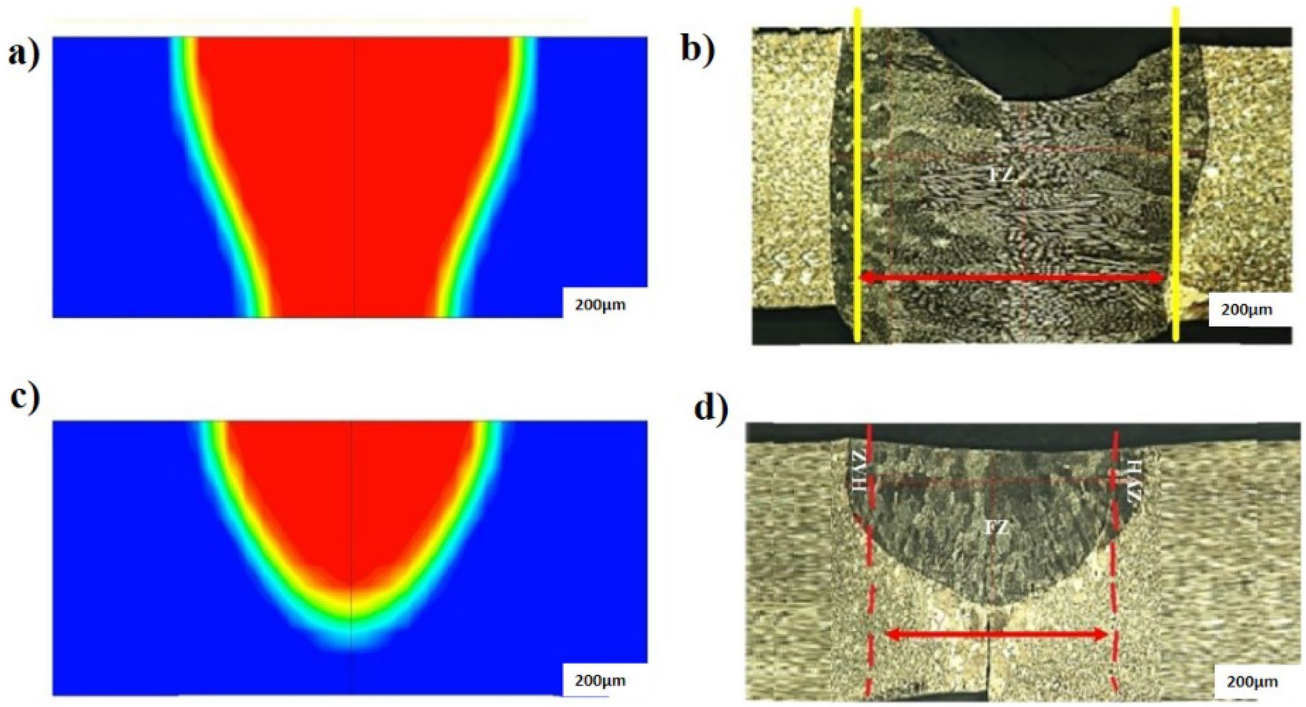

Fig. 17 Comparison of simulation results at welding speeds of (**a**) 300 mm/min and (**c**) 500 mm/min and experimental results of (**b**) 300 mm/min and (**d**) 500 mm/min for melt pool dimensions

speed and decreasing the laser power. In such a way that by enhancing the speed up to 500 mm/min, the melt has not penetrated to the depth of the workpiece.

A comparison of the simulation and experimental results can be seen in Fig. 17. At a speed of 300 mm/min, the penetration depth of the molten pool was created completely (Fig. 17a, b), and as the welding speed enhanced, the molten pool's depth and width decreased simultaneously (Fig. 17c, d). As it is observed in Fig. 17, the melt pool dimensions (width and depth) in numerical simulation are in good agreement with the experimental results.

Figure 18 indicates the changes in the width of the molten pool concerning the different welding speeds and laser powers. It can be seen that the laser power variations had a more significant effect on the width of the weld bead.

4.4 Microstructural changes of the molten pool

Figure 19 shows the variation of microstructure from the base metal to the fusion zone due to changes in a temperature gradient. As can be seen in this figure, with increasing the temperature from 700 °C to the range of 1200 and 1800 °C, microstructural changes are observed from the base metal to the HAZ region. With further increase in temperature in the molten pool to 3200 °C, the shape, size, and direction of the grains in this area have changed completely. The shape and size of the grains and the microstructure change in the molten pool area consisted of a γ

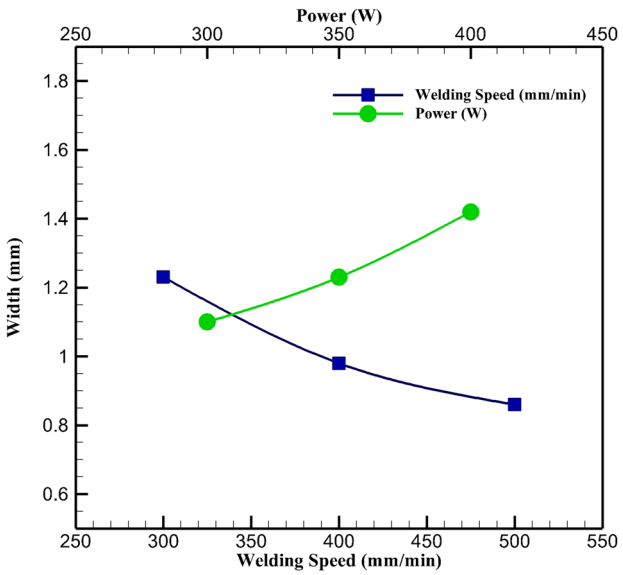

Fig. 18 The molten pool's width versus welding speed and laser power

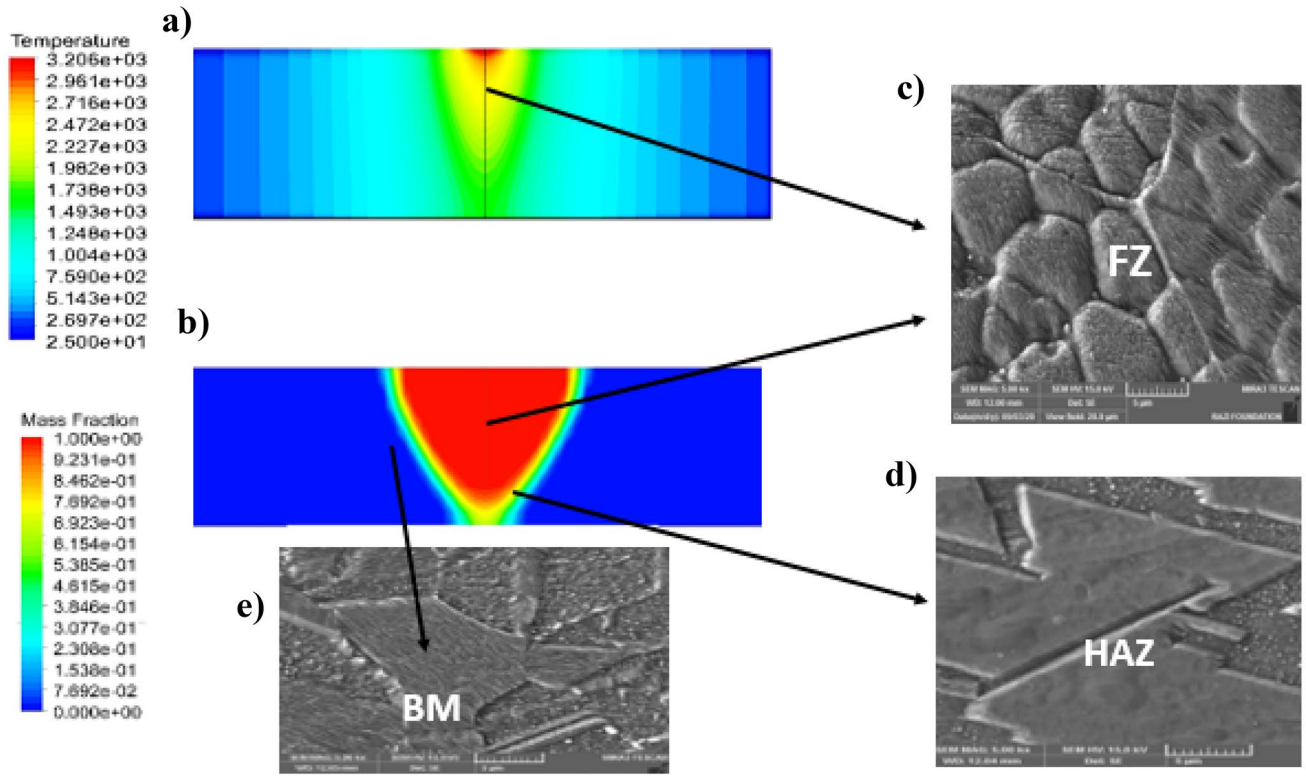

Fig. 19 Microstructural changes with temperature gradients in the molten pool area, (**a**) temperature distribution (simulation), (**b**) melting flow (simulation), (**c**) molten pool microstructure (experiment), (**d**) HAZ microstructure (experiment), and (**e**) base metal microstructure (experiment)

solid solution which increased in hardness in this area due to the intense thermal gradient. Thus, the melting of the material has led to forming a new microstructure in the fusion zone.

The temperature gradient variation in the melt pool extracted via the simulation results from 5 to 5.4S is observed in Fig. 20. This figure clearly illustrates the variation of temperature distribution at the fusion zone and adjacent areas (HAZ and base metal) at different time steps from the numerical simulation results. Figure 20a demonstrates the temperature distribution at the time of beam incident (25-mm distance from the beginning the welding or time of 5S) instantly. Afterwards, the temperature distribution at the times from 5.05S to 5.4S shown in Fig. 20b–f clearly reflects the heat dissipation through the fusion zone and base metal of the workpiece. Interestingly, the percent of peak temperature reduction rate from 5S to 5.2S was about 55% while this value was about 18% for times between 5.2S and 5.4S. It shows that the cooling rate at the center of the fusion zone has been undertake a severe reduction trend just after laser beam incident and got smoothly after 0.2S passed from the beam incident time. Hence, the microstructure change took place at this high cooling rate from the melting point to the solid-state temperature of the material. It can be concluded that the variation of intense heating from the simulation results can accurately predict the melt pool dimensions [25] and the variation of cooling cycle can predict the microstructure changes of the laser beam welding process for different metals.

Figure 21 depicts the temperature history just before and after laser irradiation point during laser welding at time period from 4 to 7 s. The temperature surged from 4S and reached to the peak value about 1 s and then sharply diminished at 0.5 s. After 5.5S, the temperature reduced gradually and reached below the 1000 °C. The heating and cooling cycle at different points imply that the center of the fusion zone to the point of 0.25 mm has had remarkable microstructural changes. The points from 0.5 to 0.75 mm have been located in the fusion line region and HAZ according to the melting point of nickel alloy (1362 °C) [38]. Moreover, the points from 0.75 to

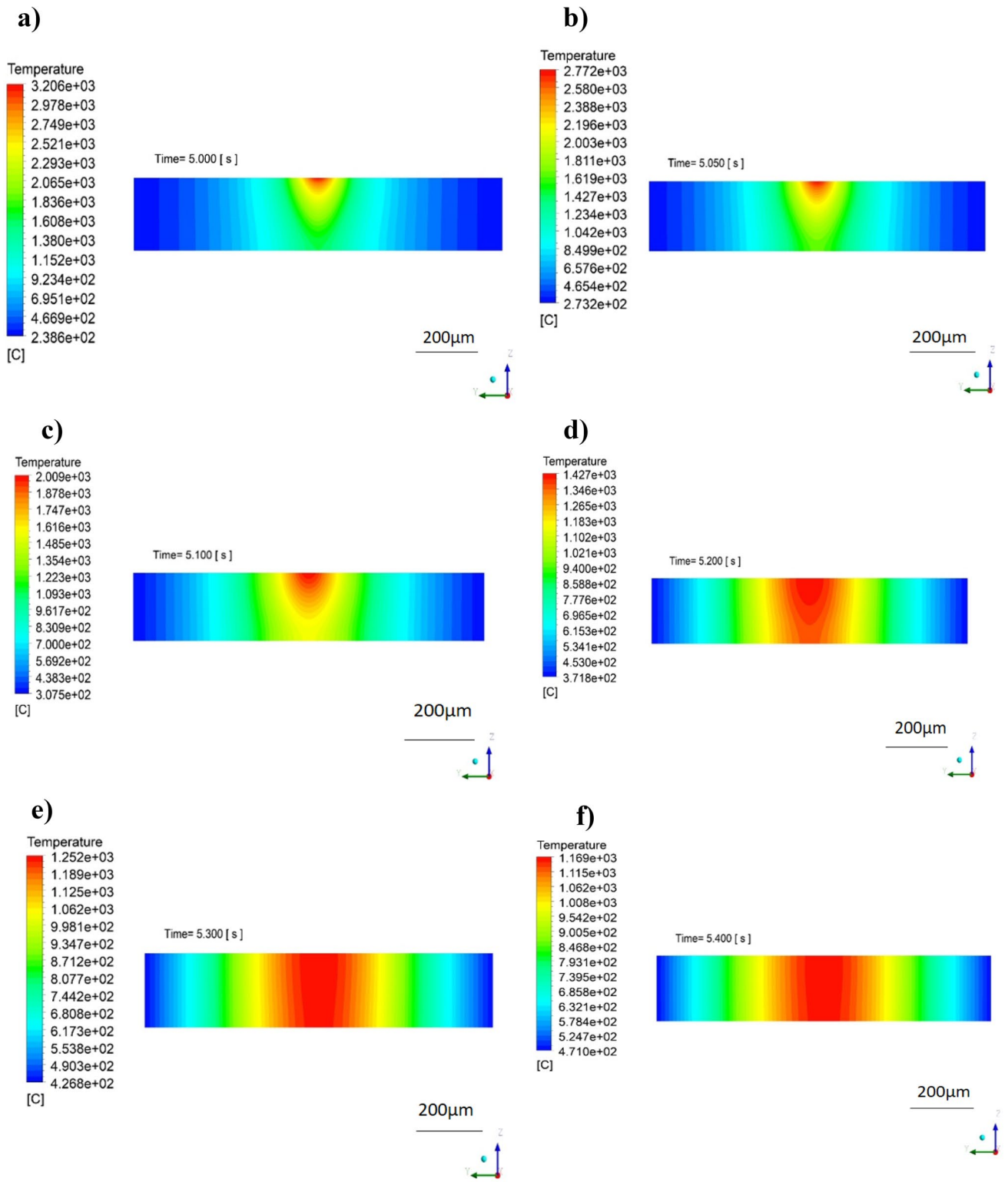

Fig. 20 Temperature distribution at welding speed of 300 mm/min and power of 400 W at 25-mm distance from the workpiece edge for different times after laser beam incident point for (**a**) 5S, (**b**) 5.05S, (**c**) 5.1S, (**d**) 5.2S, (**e**) 5.3S, and (**f**) 5.4S

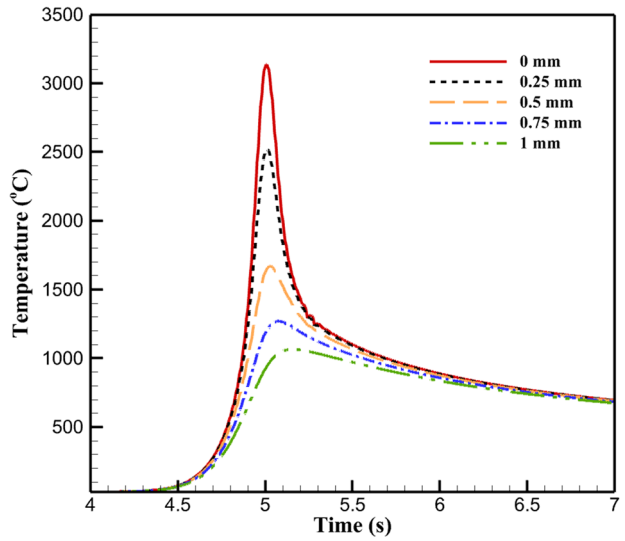

Fig. 21 Temperature history from the center of fusion zone to the base metal at different distances

1 mm experienced the peak temperature below 1362 °C which demonstrated no melting and minor microstructural changes occurred at HAZ.

As it is observed in Fig. 22a, the elemental analysis at 25 points based on the line scan energy dispersive spectroscopy (EDS) was performed. The minor changes of elements weight percentage from base metal to the HAZ and thereby fusion zone is observed in Fig. 22b. According to the phase diagram illustrated in Fig. 5, the Ni percentage for Inconel 625 was about 75 in average with small variation in different regions. Other elements such as Cr and Fe did not have evident changes while the Cr content has had slight variation in HAZ and fusion line due to experiencing higher thermal cycles. The weld metal composition was spatially homogeneous, but the concentration of Cr varied slightly. The change in the weld metal composition was much more sensitive to laser power than other parameters because of evaporation of the melted material and higher beam absorption at the fusion zone [42].

The clear microstructure change is observed in HAZ fusion line and the fusion zone as shown in Fig. 23. The fusion zone microstructure consists of columnar dendrites as a result of severe cooling effect. This structure seems to be coarser than base metal.

As it is observed in Fig. 23a, the solidification mode is changed in the fusion zone from the fusion line toward the center of the melt pool [43, 44]. The weld metal microstructure near the heat-affected zones at fusion line has a columnar dendritic structure. The solidification rate (cooling rate) in the center of fusion zone has the maximum rate whereas this value is minimum in fusion; therefor, the resultant microstructure is changed from columnar dendritic to equiaxed structure (see Fig. 23b) [45].

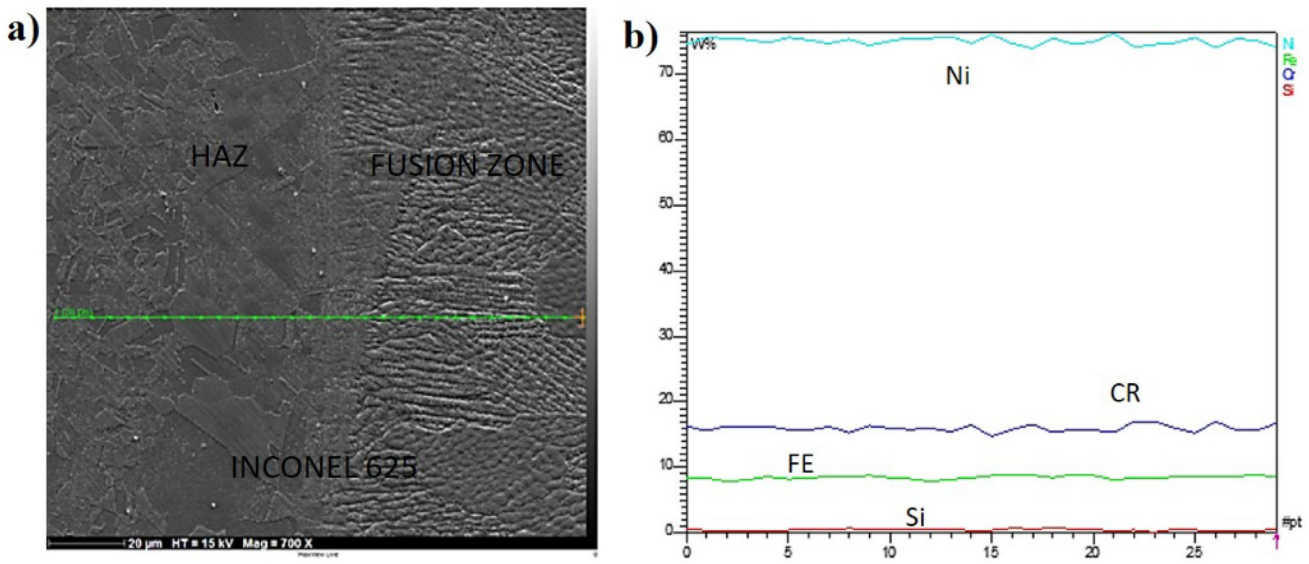

Fig. 22 Line scan energy dispersive spectroscopy (EDS) from the base metal to the fusion zone, (**a**) microstructure, (**b**) element percentage

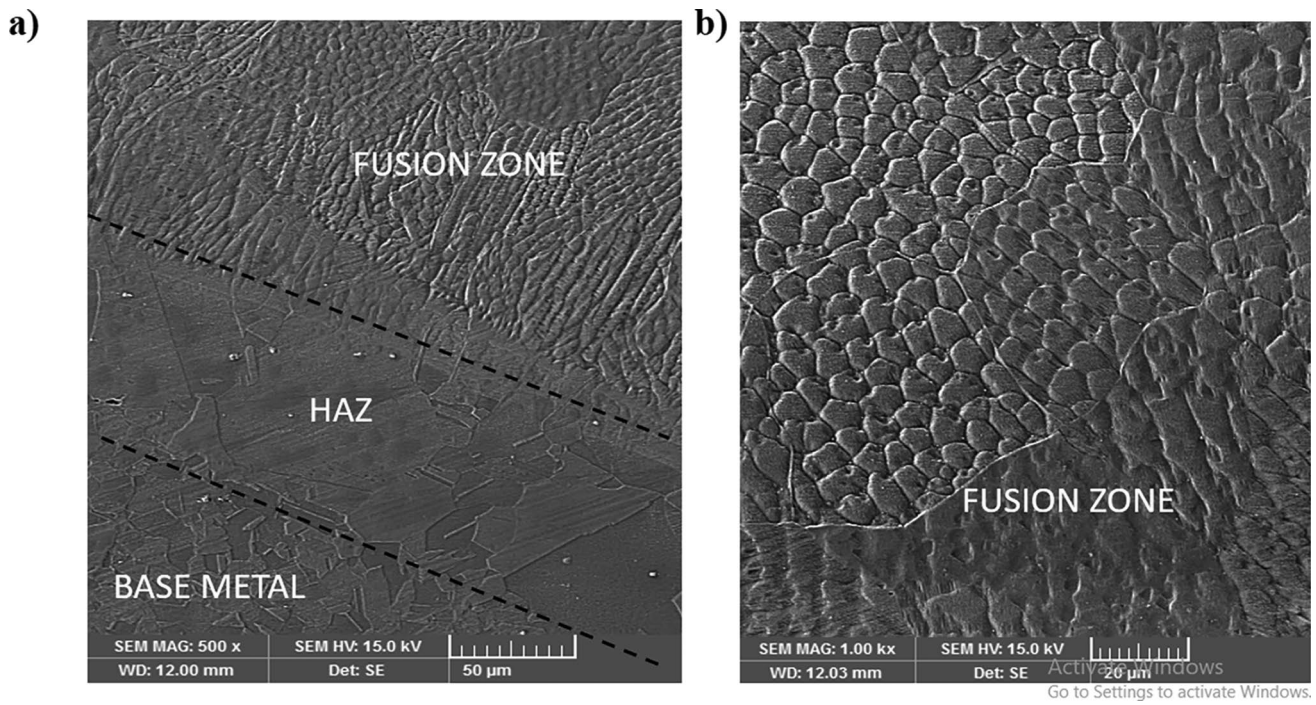

Fig. 23 Microstructural changes from the base metal to the fusion zone, (**a**) at different regions, (**b**) fusion zone

5 Conclusions

In this study, the welding speed and laser power effects during the continuous wave laser welding process of the Inconel 625 sheet were investigated by finite volume and experimental methods. In order to model the energy absorbed in the workpiece, surface and volumetric heat flux were used. Also, due to the high-temperature gradient during the welding process, the thermal conductivity, density, and specific heat capacity were defined as a function of temperature. The results are as follows:

- By enhancing the laser power from 300 to 400 W, the peak temperature in the laser beam's center at 25 mm from the beginning of the workpiece increased to 697 °C. The simulation results also showed that reducing the laser power to 300 W led to no penetration of the melt into the depth of the workpiece.
- As the welding speed increased, the constant temperature lines on the surface of the part became ellipsoid which led to a decrease in the HAZ and the melting ratio.
- Marangoni flow played a key role in determining the shape and dimensions of the molten pool so that by reducing the welding speed to 200 mm⁄min, the melt flow rate increased by 29 mm⁄s.
- By increasing the temperature from 700 °C to the range of 1200 and 1800 °C, microstructural changes have occurred from the base metal to the HAZ region, resulting in the formation of the austenitic coarse-grained structure relative to the base metal austenitic structure.

Author contribution Tlili, Sajadi, and Ghaemi conducted methodology, software, and validation; Baleanu and Sajadi conducted the experimental test and analysis of the data; Tlili, Baleanu, and Ghaemi wrote the paper; Fagiry and Tlili and Baleanu have done the revise of the paper.

Funding Dr. Iskander Tlili would like to thank Deanship of Scientific Research at Majmaah University for supporting this work under the Project No. R-2022-3.

Availability of data and material The raw/processed data required to reproduce these findings cannot be shared at this time due to technical or time limitations.

Declarations

Ethics approval Not applicable.

Consent to participate Not applicable.

Consent for publication Not applicable.

Conflict of interest The authors declare no competing interests.

References

1. Meng X, Artinov A, Bachmann M, Rethmeier M (2020) Theoretical study of influence of electromagnetic stirring on transport phenomena in wire feed laser beam welding. J Laser Appl 32(2):022026
2. Kumar GS, Saravanan S, Vetriselvan R, Raghukandan K (2018) Numerical and experimental studies on the effect of varied pulse energy in Nd:YAG laser welding of Monel 400 sheets. Infrared Phys Technol 93:184–191
3. Khdair AI, Hader M, Abushgair K, Khrais S (2021) Effect of sheet thickness on the fusion zone temperature distribution, melt pool dimensions, mechanical properties, and microstructure in laser welding of Ti6Al4V alloy. J Laser Appl 33(3):032005
4. Hu X, Xue Z, Zhao G, Yun J, Shi D, Yang X (2019) Laser welding of a selective laser melted Ni-base superalloy: Microstructure and high temperature mechanical property. Mater Sci Eng: A 745:335–345
5. Tian Z et al (2020) A review on laser powder bed fusion of Inconel 625 nickel-based alloy. Appl Sci 10(1):81
6. Liu W, Lu F, Yang R, Tang X, Cui H (2015) Gleeble simulation of the HAZ in Inconel 617 welding. J Mater Process Technol 225:221–228
7. Azari M, Rasti E, Dehkordi MHR, Azimy H, Zarei A, Bagherzadeh SA (2021) Investigation of temperature distribution and melt pool microstructure in laser fusion welding of Inconel 625 superalloy. J Laser Appl 33(2):022015
8. Faraji AH, Maletta C, Barbieri G, Cognini F, Bruno L (2021) Numerical modeling of fluid flow, heat, and mass transfer for similar and dissimilar laser welding of Ti-6Al-4V and Inconel 718. Int J Adv Manuf Technol 114(3):899–914
9. Madhankumar S et al (2021) Experimental investigation on ultimate tensile strength of laser butt welded Inconel 718 alloy and 2205 duplex stainless steel. Mater Today: Proceedings 45:6783–6787
10. Thejasree P, Manikandan N, Binoj JS, Varaprasad KC, Palanisamy D, Raju R (2021) Numerical simulation and experimental investigation on laser beam welding of Inconel 625. Mater Today: Proceedings 39:268–273
11. Ahmad GN, Raza MS, Singh NK, Kumar H (2020) Experimental investigation on Ytterbium fiber laser butt welding of Inconel 625 and duplex stainless steel 2205 thin sheets. Optics Laser Technol 126:106117
12. Voropaev A, Stramko M, Sorokin A, Logachev I, Kuznetsov M, Gook S (2020) Laser welding of Inconel 718 nickel-based alloy layer-by-layer products. Mater Today: Proceedings 30:473–477
13. Srikanth S, Parthiban A (2020) Microstructural analysis of Nd:YAG laser welding for Inconel alloy. Mater Today: Proceedings 21:568–571
14. Cheepu M, Kumar Reddy YA, Indumathi S, Venkateswarlu D (2020) Laser welding of dissimilar alloys between high tensile steel and Inconel alloy for high temperature applications. Adv Mater Process Technol 1–12
15. Sharma SK, Biswas K, Nath AK, Manna I, Majumdar JD (2020) Microstructural change during laser welding of Inconel 718. Optik 218:165029
16. Sidharth D, KV PP, Rajendran R, Narayanan S (2019) Microstructure and properties of inconel 718 and AISI 416 laser welded joints. J Mater Process Technol 266:52–62
17. Mishra A, Dixit D, Sharma AK (2018) Study on microstructural and mechanical properties of dissimilar joint of laser beam welded Inconel 625 and SS 316. Int J Eng Adv Technol 6(1):1–20
18. Li L, Peng G, Wang J, Gong J, Li H (2018) Experimental study on weld formation of Inconel 718 with fiber laser welding under reduced ambient pressure. Vacuum 151:140–147
19. Hernando I, Arrizubieta JI, Lamikiz A, Ukar E (2018) Numerical model for predicting bead geometry and microstructure in laser beam welding of Inconel 718 sheets. Metals 8(7):536
20. Hernando I, Renderos MA, Cortina M, Ruiz JE, Arrizubieta JI, Lamikiz A (2018) Inconel 718 laser welding simulation tool based on a moving heat source and phase change. Proc CIRP 74:674–678
21. Jelokhani-Niaraki MR, Mostafa Arab NB, Naffakh-Moosavy H, Ghoreishi M (2016) The systematic parameter optimization in the Nd:YAG laser beam welding of Inconel 625. Int J Adv Manuf Technol 84(9)2537–2546
22. Ebrahimi AN, Arab NBM, Gollo MH (2016) Thermal analysis of laser beam welding of nickel-based super alloy Inconel 625 to AISI 316L, using Gaussian optics theory in keyhole. J Brazilian Soc Mech Sci Eng 38(4):1199–1206
23. Janasekaran S, Tan AW, Yusof F, Abdul Shukor MH (2016) Influence of the overlapping factor and welding speed on T-joint welding of Ti6Al4V and Inconel 600 using low-power fiber laser. Metals 6(6):134
24. Ren W, Lu F, Yang R, Liu X, Li Z, Hosseini SRE (2015) A comparative study on fiber laser and CO2 laser welding of Inconel 617. Mater Des 76:207–214
25. Duggirala A, Kalvettukaran P, Acherjee B, Mitra S (2021) Numerical simulation of the temperature field, weld profile, and weld pool dynamics in laser welding of aluminium alloy. Optik 247:167990
26. Kik T (2020) Heat source models in numerical simulations of laser welding. Materials 13(11):2653
27. Artinov A, Bachmann M, Rethmeier M (2018) Equivalent heat source approach in a 3D transient heat transfer simulation of full-penetration high power laser beam welding of thick metal plates. Int J Heat Mass Transf 1(122):1003–1013
28. Ducharme R, Kapadia P, Dowden J (1992) A mathematical model of the defocusing of laser light above a workpiece in laser material processing. Int Congr Appl Lasers Electro Opt 1992:187–197
29. Abderrazak K, Bannour S, Mhiri H, Lepalec G, Autric M (2009) Numerical and experimental study of molten pool formation during continuous laser welding of AZ91magnesium alloy. Comput Mater Sci 44:858–866
30. Kundakcıoğlu E, Lazoglu I, Poyraz Ö, Yasa E, Cizicioğlu N (2018) Thermal and molten pool model in selective laser melting process of Inconel 625. Int J Adv Manuf Technol 95(9):3977–3984
31. Kaschnitz E, Kaschnitz L, Heugenhauser S (2019) Electrical resistivity measured by millisecond pulse heating in comparison with thermal conductivity of the superalloy Inconel 625 at elevated temperature. Int J Thermophys 40(3):27
32. O'Flynn J, Whitman CA, Corbin SF (2020) Thermal property measurements of metal injection moulded Inconel 625 and Inconel 718 using combined thermal analysis techniques. Powder Metall 63(4):277–287
33. Wang Z, Denlinger E, Michaleris P, Stoica AD, Ma D, Beese AM (2017) Residual stress mapping in Inconel 625 fabricated through additive manufacturing: method for neutron diffraction measurements to validate thermomechanical model predictions. Mater Des 5(113):169–177
34. Özel T, Arısoy YM, Criales LE (2016) Computational simulation of thermal and spattering phenomena and microstructure in selective laser melting of inconel 625. Phys Procedia 1(83):1435–1443
35. Mills KC (2002) Recommended values of thermophysical properties for selected commercial alloys. Woodhead Publishing
36. Quested PN, Valencia JJ (2010) Thermophysical properties
37. Indhu R, Vivek V, Sarathkumar L, Bharatish A, Soundarapandian S (2018) Overview of laser absorptivity measurement techniques for material processing. Lasers Manuf Mater Process 5(4):458–481
38. Singleton MF, Nash P (1991) Phase diagrams of binary nickel alloys. ASM International, Materials Park 1991:207–212

39. Dhahri M, Masse JE, Mathieu JF, Barreau G, Autric M (2001) Laser welding of AZ91 and WE43 magnesium alloys for automotive and aerospace industries. Adv Eng Mater 3(7):504–507
40. Lee JY, Ko SH, Farson DF, Yoo CD (2002) Mechanism of keyhole formation and stability in stationary laser welding. J Phys D Appl Phys 35(13):1570
41. Rosenthal D (1946) Transactions of ASME 68:849–866
42. Liu T, Yang LJ, Wei HL, Qiu WC, Debroy T (2017) Composition change of stainless steels during keyhole mode laser welding. Weld J 1(96):258–270
43. Kou S (2003) Welding metallurgy, 2nd edn. Jon Wily & Sons Inc, Hoboken
44. Winegard WC (1994) An introduction to the solidification of metal. Institute of Metals
45. Pang M, Yu G, Wang HH, Zheng CY (2008) Microstructure study of laser welding cast nickel-based superalloy K418. J Mater Process Technol 207(1–3):271–275